Nanoscale

PAPER

View Article Online
View Journal | View Issue

Cite this: *Nanoscale*, 2019, **11**, 17478

Coordination polymer derived general synthesis of multi-shelled hollow metal oxides for lithium-ion batteries†

Dongyang Xue, ‡ Fangfang Xue,‡ Xiaoping Lin, Fengyi Zong, Jianmin Zhang and Qiuhong Li *

Received 19th June 2019,
Accepted 25th August 2019

DOI: 10.1039/c9nr05220h

rsc.li/nanoscale

Multi-shelled hollow metal oxide nanostructures have attracted tremendous attention in energy storage devices owing to their high specific capacity, rate capability and ameliorated cycling performance. Although great progress has been made in synthesizing multi-shelled hollow structures, most methods still depend on tedious template mediated strategies to generate complex interior structures. Herein, we developed a facile universal self-templated approach to synthesize a series of multi-shelled hollow metal oxide spheres with tailored compositions. This strategy involved the solvothermal preparation of uniform spherical coordination polymers (CPs) as precursors and a subsequent thermal treatment in air. Single-, binary- and ternary-metal multi-shelled hollow oxide spheres (Co, Mn–Co, Ni–Co–Mn, *etc.*) were successfully obtained. To demonstrate their applications in energy storage, the electrochemical properties of $ZnCo_2O_4$ were investigated by testing the lithium-ion-storage performance. Owing to the unique structures, the multi-shelled hollow $ZnCo_2O_4$ spheres exhibited high specific capacity, excellent cycling durability (1200 mA h g^{-1} after 200 cycles at 0.1 A g^{-1}) and prominent rate capability (730 mA h g^{-1} at 5.0 A g^{-1}).

Introduction

Hollow nanostructures, a family of special nanomaterials with well-defined solid shells and inner voids, have attracted considerable interest due to their unique structural features.[1–4] In recent decades, owing to their high specific surface area, short charge transport path and tunable chemical composition, this family has found versatile applications in energy storage and conversion, catalysis, gas sensing, photocatalysis, biomedicine and so forth.[5–10]

Among various hollow structures, multi-shelled hollow nanomaterials (MSHMs) are much more interesting because of the synergistic effect of the adjacent shells.[11] Recently, multi-shelled hollow nanostructures, composed of multiple boundaries and multiple interior cavities, have been regarded as promising electrode materials in lithium-ion batteries (LIBs) to improve the electrochemical performance by effectively relieving volume expansion during repeated Li^+ insertion/deinsertion processes.[12–15] Over the past two decades, hollow nanostructures have been successfully synthesized by conventional hard or soft templating methods.[2] Among them, multi-shelled nanostructures were more difficult to synthesize than single-shelled or double-shelled ones due to their complex structures. In recent years, MSHMs have been constructed by using templates such as carbon, polystyrene, silicon, vesicles, micelles, microemulsions, *etc.*[16–22] Nevertheless, these template mediated strategies require tedious procedures and consume a lot of time and resources. Also, the number of shells is limited by the diffusion and deposition of metal cations on the template. Therefore, it is necessary to develop facile non-templated or self-templated methods based on different mechanisms, such as surface-protected etching,[23–25] galvanic replacement,[26–28] Ostwald ripening[29–31] and Kirkendall effect.[32–34]

In order to study the formation of hollow nanostructures, many materials have been investigated as precursors. Coordination polymers (CPs), a novel class of materials composed of metal ions and organic ligands,[35–37] have been considered to be a promising precursor to generate hollow nanostructures. For example, Lou's group synthesized multishelled Ni–Co oxide particles using amorphous coordination polymer spheres (CPSs) as the precursors.[38] Oh and co-workers demonstrated a strategy for the synthesis of multicomponent ball-in-ball hybrid metal oxides by taking advantage of the ion exchange and thermal behavior of CPSs.[39] In spite of the outstanding achievement, it is still a great challenge to explore

Pen-Tung Sah Institute of Micro-Nano Science and Technology, Xiamen University, Xiamen, China. E-mail: liqiuhong@xmu.edu.cn; Fax: +86-0592-2187196; Tel: +86-0592-2187198

†Electronic supplementary information (ESI) available. See DOI: 10.1039/c9nr05220h

‡These authors contributed equally to this work.

facile and universal approaches, which can be applied to obtain binary or ternary metal oxides with complicated multi-shelled nanostructures.

Herein, we have developed a facile general strategy to synthesize multi-shelled hollow metal oxides with amorphous CPs as precursors. This strategy involves the solvothermal preparation of uniform CPs and subsequent thermal calcination in air. The amorphous CPs are synthesized through using *p*-phthalic acid (PTA) as organic ligands, transition metal ions as metallic nodes, and *N*,*N*-dimethylformamide (DMF)/glycerol as a mixed solvent. Pretty uniform multi-shelled hollow $ZnCo_2O_4$ spheres are synthesized without any other template. We demonstrate the universality of this strategy by synthesizing several other compositions with multi-shelled interior structures. When evaluated as anode electrode materials for LIBs, the multi-shelled hollow $ZnCo_2O_4$ spheres manifest high capacity, outstanding cycling stability and excellent rate performance.

Results and discussion

The schematic growth of multi-shelled hollow spheres (MSHSs) is shown in Scheme 1. Using $ZnCo_2O_4$ as an example, we synthesized Zn–Co CPs as the precursor, from the deposition of Zn^{2+} and Co^{2+} cations in the presence of PTA as the organic ligand through a solvothermal process. A homogenous pink solution was prepared. Scanning electron microscopy (SEM) and transmission electron microscopy (TEM) are used to characterize the precursors collected at different stages. During the solvothermal reaction, the CP sheets are firstly formed by the coordinating interaction between metal ions (Zn^{2+} and Co^{2+}) and PTA (Fig. S1a and d†). Multiple coordination bonds between PTA molecules and metal ions motivate them to cross-link with each other to form CPs. As the reaction proceeds, glycerol in the mixed solution will further stimulate the self-assembly process of CP sheets by acting as a cross-link agent,[40] leading to the formation of urchin-like hollow microspheres (Fig. S1b and e†). The hydroxyl groups of glycerol are covalently bonded with carboxyl groups on the surface of CP sheets, and promote the agglomeration of CP sheets. Ultimately, the dehydration condensation of hydroxyl groups leads to the formation of self-assembled microspheres with uniformly distributed metal ions and expanded volume during the solvothermal treatment. With a longer reaction time, the hollow microspheres composed of nanosheets gather inward to form an interior core, meanwhile, some other nanosheets self-assemble to form an outer shell. After solvothermal treatment for 6 h, yolk-shelled Zn–Co CPs are obtained (Fig. S1c and f†). Subsequently, a simple heat treatment is applied and $ZnCo_2O_4$ MSHSs are successfully formed without any template. The unique multi-shell structure is formed during the simultaneous action of contraction and adhesion forces.[41] The inner layers are converted from the inward shrinkage of the spherical precursor core caused by the contraction force. Meanwhile, the outer shell is hindered from inward shrinkage by the adhesion force.

The morphology, structure and composition of Zn–Co CPs and Zn–Co oxide MSHSs are investigated. As shown in Fig. 1a, the low magnification SEM image shows that the precursors are well-defined urchin-like microspheres with an average diameter of about 1.5 μm. Magnified SEM images in Fig. 1b and c display nanoflakes over the entire particle surface and hollow core–shell structure. Control experiments were carried out to verify the role of glycerol on the structure of the precursors. Fig. S2a and b† show that the prepared samples without PTA exhibit a fusiform morphology composed of nanosheets, which is different from the morphology of Zn–Co CPs. When we just use DMF (45 mL) as the solvent (Fig. S2c and d†), the control products are not uniform with irregular morphologies. Therefore, only under the glycerol condition, we can obtain regular microspheres. The powder X-ray diffraction (XRD) pattern indicates the amorphous nature of the Zn–Co CPs (Fig. S3†). The Fourier transform infrared spectrum reveals that the wave number of C=O stretching shifts from 1685 to 1584 cm^{-1} after the synthesis of Zn–Co CPs, demonstrating the coordination of carboxylate groups of PTA to metal ions (Zn^{2+} and Co^{2+}) (Fig. 2a).[38] The Zn–Co CPs are transformed into multi-shelled hollow microspheres by a slow radial temperature gradient. During the oxidation progress, the formation of inner space is ascribed to the considerable mass loss

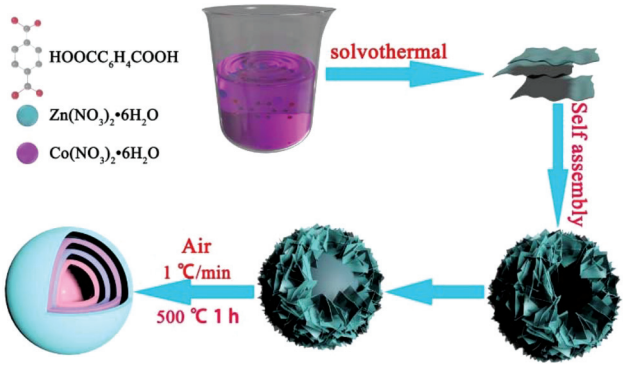

Scheme 1 Schematic illustration of the synthesis process of multi-shelled hollow spheres.

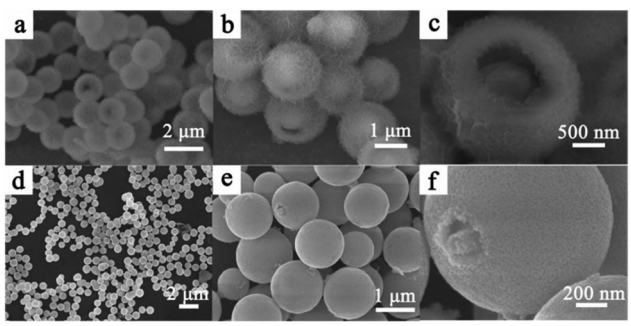

Fig. 1 (a–c) SEM images of Zn–Co CPs at different magnifications, (d–f) SEM images of $ZnCo_2O_4$ MSHSs at different magnifications.

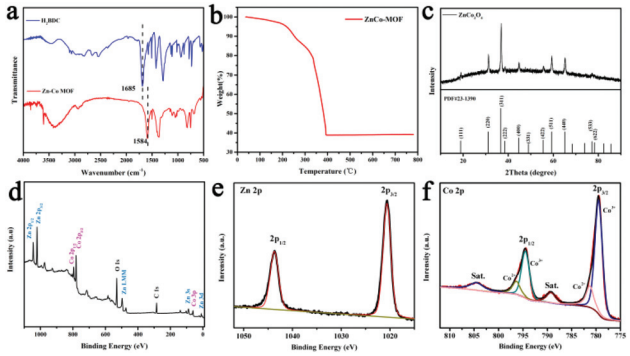

Fig. 2 (a) FTIR spectra of Zn–Co CPs and *p*-phthalic acid (PTA); (b) thermogravimetric analysis profile of Zn–Co CPs; (c) XRD patterns of $ZnCo_2O_4$ MSHSs; XPS spectra of $ZnCo_2O_4$ MSHSs: (d) survey spectrum and high-resolution (e) Zn 2p and (f) Co 2p.

(~60%, Fig. 2b) caused by the oxidation of organic ligands. After heat treatment, Zn–Co CPs are converted into a uniform spherical shape with a relatively rough surface (Fig. 1d–f). Moreover, the high magnification SEM image exhibits that the surface of Zn–Co oxides is composed of small nanograins with an average size of 15 nm. The morphology of Zn–Co oxides is further investigated by TEM. As shown in Fig. 3a–c, TEM images of Zn–Co oxides indicate that each as-synthesized sphere basically possesses a unique six-layered hollow structure. The HRTEM images of Zn–Co oxides shown in Fig. 3d and e reveal three groups of lattice fringes with interplanar spacings of 0.24 nm, 0.28 nm and 0.465 nm, which can be ascribed to the (311), (220) and (111) planes of the spinel $ZnCo_2O_4$ phase, respectively. The selected area electron diffraction (SAED) image (Fig. 3f) clearly demonstrates the polycrystalline structure of the

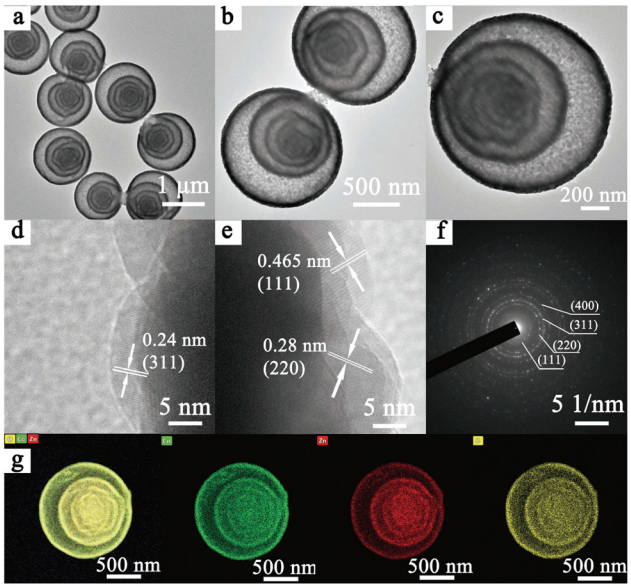

Fig. 3 (a–c) TEM images of $ZnCo_2O_4$ MSHSs in different resolutions, (d and e) HRTEM images, (f) SAED pattern, and (g) EDS mapping images of $ZnCo_2O_4$ MSHSs.

$ZnCo_2O_4$ MSHSs and the diffraction rings can be easily matched with the spinel $ZnCo_2O_4$ phase.

As shown in Fig. 2c, the XRD pattern of Zn–Co oxides reveals crystallinity and phase structure information of the synthesized sample. All the diffractions of Zn–Co oxides are well indexed to the standard pattern of the spinel $ZnCo_2O_4$ phase, which is consistent with the HRTEM and SAED results. Meanwhile, the results of energy-dispersive spectroscopy (EDS) mapping results are shown in Fig. 3g. From the mapping images of Co, Zn, and O elements, it can be seen that each element is uniformly distributed in every layer. EDS analysis shows that Zn/Co atomic ratio of $ZnCo_2O_4$ MSHS is about 1 : 2 (Fig. S4†). X-ray photoelectron spectroscopy (XPS) is introduced to further investigate the oxidation state of transition metal ions in $ZnCo_2O_4$ MSHSs. As shown in Fig. 2d, the full wide scan spectrum of $ZnCo_2O_4$ MSHSs reveals the presence of Zn, Co, and O elements. The high resolution XPS spectra of Zn 2p and Co 2p after Gaussian fitting are shown in Fig. 2e and f. In the Zn 2p spectrum (Fig. 2e), two distinct peaks located at 1020.6 and 1043.7 eV are assigned to Zn $2p_{3/2}$ and Zn $2p_{1/2}$ levels, respectively, indicating the characteristic peak of Zn^{2+}.[42] The deconvoluted Co 2p spectra (Fig. 2f) show two strong peaks at 779.5 and 794.5 eV corresponding to Co $2p_{3/2}$ and Co $2p_{1/2}$, respectively, with a spin–orbit splitting of around 15 eV, owing to the mixed Co^{2+} and Co^{3+} ions.[42,43]

To investigate the universality of the self-templated method, Co_3O_4, ZnO–$ZnCo_2O_4$, Mn–Co, Ni–Co, and Ni–Mn oxide MSHSs have been synthesized by changing the spices and mole ratio of metal ions. In Fig. 4, SEM and TEM images of Co_3O_4 clearly reveal outstanding uniformity and a similar mor-

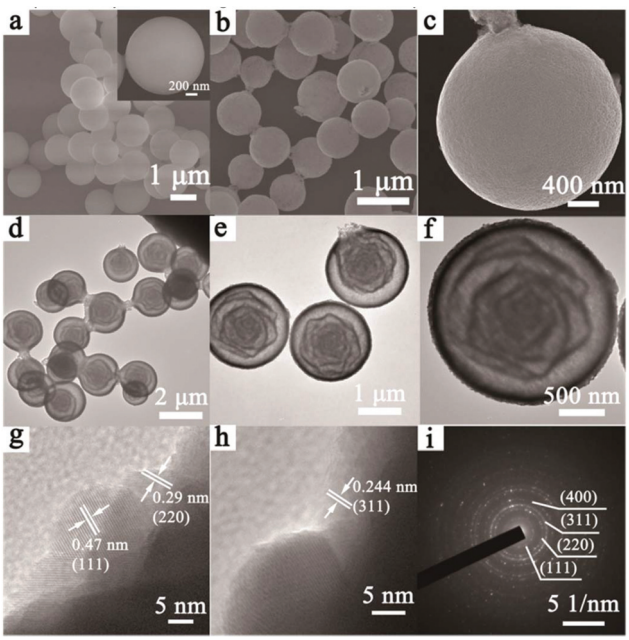

Fig. 4 (a) SEM image of Co CPs; (b and c) SEM images of Co_3O_4 MSHSs at different magnifications; (d–f) TEM images of Co_3O_4 MSHSs at different magnifications; (g and h) HRTEM images and (i) SAED pattern of Co_3O_4 MSHSs.

phology to $ZnCo_2O_4$ MSHSs. After thermal treatment, Co CPs exhibit uniform spherical shapes with a smooth surface (Fig. 4a), indicating that the spheres consist of generous nanograins (Fig. 4b). In addition, the diameter of Co_3O_4 is reduced to about 1.2 μm (Fig. 4c), which is smaller than Co CPs because of the shrinkage during the heat treatment. As shown in Fig. 4d–f, TEM images of Co_3O_4 in various resolutions show that Co_3O_4 spheres possesses at least four layers. The HRTEM images (Fig. 4g and h) indicate three groups of lattice fringes with interplanar spacings of 0.47 nm, 0.29 nm and 0.244 nm respectively, which is well consistent with the (111), (220) and (311) planes of cubic Co_3O_4, respectively. The SAED result (Fig. 4i) evidently confirms the polycrystalline texture of Co_3O_4 MSHSs and the diffraction rings can be easily matched with the cubic Co_3O_4 phase.

Fig. S5† reveals the morphology of the Mn–Co, Ni–Co and Ni–Mn CPs. As expected, the morphology of the three bimetallic CPs is similar with a uniform spherical shape. As shown in Fig. S5a and b,† Mn–Co CPs are urchin-like microspheres by the assembly of nanosheets with an average diameter of about 1.5 μm. The as-synthesized Ni–Co CPs are also urchin-like microspheres composed of nanosheets and the diameter was about 800 nm (Fig. S5c and d†). As shown in Fig. S5e and f,† the SEM images of Ni–Mn CPs indicate that the as-prepared precursors possess a uniform spherical morphology with a smooth surface. After the thermal treatment in air, these bimetallic CPs are converted into binary metal oxides. The morphology and structure of these binary metal oxides are examined by SEM and TEM. Fig. 5a–c evidently confirm that the Mn–Co oxides possess a four-layered hollow structure with a uniform size of about 1.5 μm. Ni–Co (Fig. 5d–f) and Ni–Mn (Fig. 5g–i) oxides also reveal a similar morphology and internal architecture. In order to further prove the adjustability of element ratio of the MSHSs, ZnO–$ZnCo_2O_4$ MSHSs with a controlled Zn/Co molar ratio of 1 : 1 are successfully synthesized. As shown in Fig. S6a,† the morphology of ZnO–$ZnCo_2O_4$ MSHSs is similar to that of $ZnCo_2O_4$ MSHSs. From the TEM images (Fig. S6b and c†) of ZnO–$ZnCo_2O_4$ MSHSs, the four-layered interior structure can be easily observed. EDS element mapping (Fig. S6d†) images also confirm the uniform element distribution in ZnO–$ZnCo_2O_4$ MSHSs. XRD is employed to further confirm the crystal structure and chemical compositions of these multi-shelled metal oxides. As shown in Fig. S7,† all the diffraction peaks of these multi-shelled metal oxides are well matched with the corresponding standard PDF cards, respectively. Furthermore, we also synthesized several ternary metal oxides (Mn–Co–Zn, Ni–Co–Zn and Ni–Co–Mn) with a multi-shelled hollow structure. The SEM images in Fig. 6a, d and g distinctly show that these ternary metal oxides are spherical with a rough surface. As shown in Fig. 6b, c, e, f, h, and i, TEM images of Mn–Co–Zn, Ni–Co–Zn, and Ni–Co–Mn oxides display a uniform spherical shape with a four, three, and six-layered hollow structure, respectively. EDS is applied to verify the chemical compositions of these ternary metal oxides (Fig. S8†). Based on the above results, various multi-shelled hollow metal oxides are successfully obtained, demonstrating the generality of our synthesis strategy.

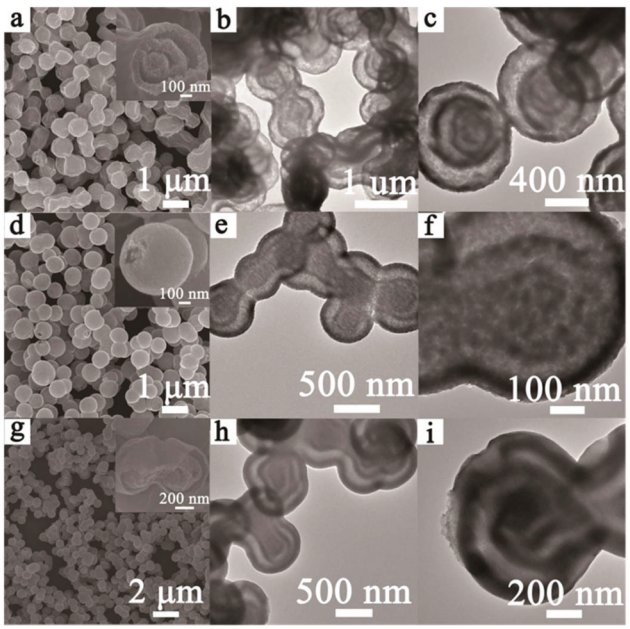

Fig. 5 (a) SEM image of Mn–Co oxides; (b and c) TEM images of Mn–Co oxides at different magnifications; (d) SEM image of Ni–Co oxides; (e and f) TEM images of Ni–Co oxides at different magnifications; (g) SEM image of Ni–Mn oxides; (h and i) TEM images of Ni–Mn oxides at different magnifications.

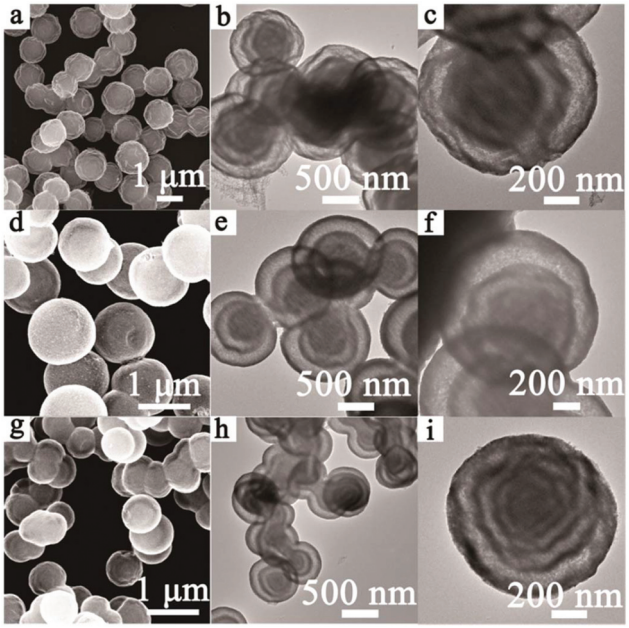

Fig. 6 (a) SEM image of Mn–Co–Zn oxides; (b and c) TEM images of Mn–Co–Zn oxides at different magnifications; (d) SEM image of Ni–Co–Zn oxides; (e and f) TEM images of Ni–Co–Zn oxides at different magnifications; (g) SEM image of Ni–Co–Mn oxides; (h and i) TEM images of Ni–Co–Mn oxides at different magnifications.

The multi-shelled hollow structures are promising in various applications. In this work, we have studied their potential application in lithium ion batteries. The electrochemical properties of the as-synthesized $ZnCo_2O_4$ MSHSs are demonstrated by cyclic voltammetry (CV) and galvanostatic charge/discharge cycling testing. Fig. 7a exhibits the initial five CV curves of the $ZnCo_2O_4$ MSHS anode in a voltage range from 0.01 to 3.0 V at a scanning rate of 0.1 mV s^{-1}. It is noteworthy that there is a big difference in the first cycle compared with the other four cycles. In the first cathodic scan, a pronounced reduction peak can be easily observed. The peak located at 0.7 V is attributed to the decomposition of $ZnCo_2O_4$ to metallic Zn and Co and the transition of Li to amorphous Li_2O together with the formation of a solid electrolyte interphase (SEI) film.[44,45] In the first anodic scan, two distinct oxidation peaks at 1.68 V and 2.08 V can be ascribed to the oxidation of metallic Zn and Co to Zn^{2+} and Co^{3+}, accompanied by the decomposition of Li_2O to form lithium, which confirms the reversibility of this redox reaction. In the second cycle, the reduction peak shifts to higher potentials (0.7 to 1.07 V) together with sharply decreased intensity, corresponding to some irreversible reaction during the discharge process in the first cycle. Apparently, all peaks of the subsequent CV curves are well overlapped, which further indicates the reversibility and stability of the electrochemical reaction during the charge/discharge process.

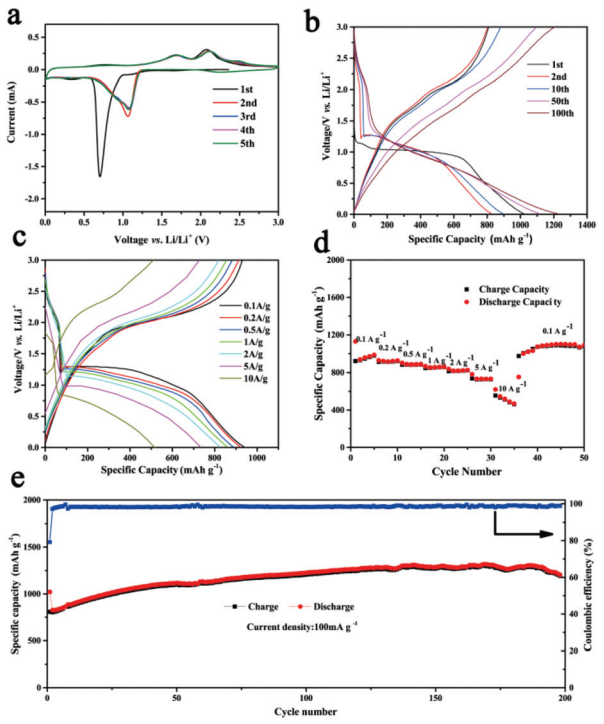

Fig. 7 (a) CV curves of $ZnCo_2O_4$ MSHSs at a scan rate of 0.1 mV s^{-1} in the potential range from 0.01 to 3.0 V; (b) charge–discharge curves of $ZnCo_2O_4$ MSHSs at a current density of 100 mA g^{-1}; (c) charge–discharge curves of $ZnCo_2O_4$ MSHSs at different current densities; (d) rate performance of $ZnCo_2O_4$ MSHSs; (e) cycling performance of $ZnCo_2O_4$ MSHSs at a current density of 100 mA g^{-1}.

Based on the above CV analysis and previous reports, the electrochemical process of the $ZnCo_2O_4$ electrode can be expounded as follows:

$$ZnCo_2O_4 + 8Li^+ + 8e^- \rightarrow Zn + 2Co + 4Li_2O \quad (1)$$

$$Zn + Li^+ + e^- \leftrightarrow LiZn \quad (2)$$

$$Zn + Li_2O \leftrightarrow ZnO + 2Li^+ + 2e^- \quad (3)$$

$$2Co + 2Li_2O \leftrightarrow 2CoO + 4Li^+ + 4e^- \quad (4)$$

$$2CoO + 2/3Li_2O \leftrightarrow 2/3Co_3O_4 + 4/3Li^+ + 4/3e^- \quad (5)$$

Fig. 7b shows the galvanostatic charge/discharge properties of $ZnCo_2O_4$ MSHSs at 100 mA g^{-1} over a potential range from 0.01 V to 3.0 V. There is a distinct voltage plateau at about 1.05 V in the first discharge process, which can be attributed to the decomposition of $ZnCo_2O_4$ to metallic Zn and Co and the formation of the SEI film, fitting with the CV curves. In the subsequent cycles, the potential plateau shifts near to 1.25 V, corresponding to the polarization of electrode materials and the structural and compositional restoration. As shown in Fig. 7b, the discharge/charge curves of 2^{nd}, 10^{th}, 50^{th}, 100^{th} are shifting to the right gradually, indicating that the specific capacity of the $ZnCo_2O_4$ MSHS electrode gradually increases during the following discharge/charge process.

A multiple-step galvanostatic strategy is chosen to further investigate the rate performance of $ZnCo_2O_4$ MSHSs and the results are shown in Fig. 7c and d. Fig. 7c demonstrates the discharge/charge curves of $ZnCo_2O_4$ MSHSs at different current densities ranging from 0.1 to 10 A g^{-1}. Based on the analysis of the curves at various current densities, it can be seen that the discharge potential decreases and charge potential increases with the rise of discharge/charge current densities, corresponding to the kinetic effect of the electrode material. As shown in Fig. 7d, the $ZnCo_2O_4$ MSHS electrode displays remarkable rate performance. The $ZnCo_2O_4$ MSHS electrode delivers a high reversible capacity of 970, 920, 888, 860, 820 and 730 mA h g^{-1} at current densities of 0.1, 0.2, 0.5, 1.0, 2.0 and 5.0 A g^{-1}, respectively. When the current density is further increased to 10 A g^{-1}, the specific capacity evidently decreases and still retains 450 mA h g^{-1}. More importantly, when the current density is turned back to 0.1 A g^{-1}, the specific capacity is reversibly back to 1020 mA h g^{-1}, indicating the excellent rate performance of $ZnCo_2O_4$ MSHSs.

As shown in Fig. 7e, the cycling performance of the $ZnCo_2O_4$ MSHS electrode is studied at a current density of 100 mA g^{-1} in the potential range from 0.01 V to 3.0 V. The $ZnCo_2O_4$ MSHS electrode exhibits initial discharge and charge capacities of 1020 and 809 mA h g^{-1} respectively, corresponding to an initial coulombic efficiency of 79.25%. The 20.75% irreversible capacity loss is mainly ascribed to the formation of the SEI film in the first discharge process. It is easy to observe from the figure that the capacity of $ZnCo_2O_4$ MSHSs gradually increases with the cycling. The capacity of $ZnCo_2O_4$ MSHSs increases from initial 809 to 1300 mA h g^{-1}. It is probably caused by the gradual active process of multi-shell struc-

tures of transition metal oxides. After 200 cycles, the $ZnCo_2O_4$ MSHS electrode still retains a capacity of 1200 mA h g^{-1}, indicating the excellent cycling properties of $ZnCo_2O_4$ MSHSs. The electrochemical performance of $ZnCo_2O_4$ MSHSs is superior to many other Zn–Co based metal oxides (Table S1†), which can be related to the advantageous structural features of the multi-shelled hollow metal oxides.

The superior lithium-ion-storage performance of $ZnCo_2O_4$ MSHSs can be attributed to the synergism of their complex multi-shelled structure and interfacial-storage effect.[46–48] The multi-shelled hollow structures provide abundant electrochemical active sites and alleviate volume expansion of electrode materials during the discharge/discharge process. In addition, each shell with high porosity is composed of a large number of nanograins, which can shorten ion-diffusion lengths.[49,50] The unique multi-shelled interior structures offer more reaction interfaces during the lithium-storage process, which enhances the specific capacity of electrode materials.

To further display the electrochemical properties of multi-shelled metal oxides, Co_3O_4 MSHSs are also evaluated. The CV, charge–discharge rate and cycling curves are given in Fig. S9 (a–d).† The Co_3O_4 MSHS electrode exhibits high reversible capacities of 944, 1010, 906, 897, 869, 813, and 720 mA h g^{-1} at current densities of 0.1, 0.2, 0.5, 1.0, 2.0, and 5.0 A g^{-1} respectively. When the current density is returned to 0.1 A g^{-1}, the specific capacity is reversibly back to 1100 mA h g^{-1} after 10 cycles. The electrode also shows excellent cyclic life at a current density of 500 mA g^{-1}. The capacity increases gradually from 849 to 1380 mA h g^{-1} and still retains a capacity of 1300 mA h g^{-1} after 100 cycles. These results indicate that Co_3O_4 MSHSs possess a similar superior electrochemical performance as $ZnCo_2O_4$ MSHSs.

Conclusions

In summary, we have developed a general self-templated method to synthesize complex multi-shelled metal oxide microspheres with a tailored chemical composition. We introduce glycerol as a crosslinking agent in solvents to synthesize spherical CPs to serve as precursors, and multi-shelled metal oxide microspheres are generated after a facile thermal treatment. To verify the universality of this method, various multi-shelled hollow microspheres with different chemical compositions are successfully synthesized. The $ZnCo_2O_4$ MSHSs and Co_3O_4 MSHSs are adopted as anode materials for LIBs, which deliver high specific capacities, excellent cycling performances and superior rate capabilities. In this work, we have provided a facile and novel way to prepare multi-shelled metal oxide microspheres, which will be promising not only in lithium-ion-storage, but also in a wide range of other fields.

Conflicts of interest

There are no conflicts to declare.

Acknowledgements

This work was partly supported by the National Natural Science Foundation of China (Grant No. 61574118), and the Key Project of Science and Technology Plan of Fujian Province (Grant No. 2015H0038).

Notes and references

1 X. J. Wang, J. Feng, Y. C. Bai, Q. Zhang and Y. D. Yin, *Chem. Rev.*, 2016, **116**, 10983–11060.
2 X. W. Lou, L. A. Archer and Z. C. Yang, *Adv. Mater.*, 2008, **20**, 3987–4019.
3 L. Yu, X. Y. Yu and X. W. (David) Lou, *Adv. Mater.*, 2018, **30**, 1800939.
4 Y. Lu, L. Yu and X. W. (David) Lou, *Chem*, 2018, **4**, 972–996.
5 L. Yu, H. B. Wu and X. W. D. Lou, *Acc. Chem. Res.*, 2017, **50**, 293–301.
6 L. Yu, H. Hu, H. B. Wu and X. W. Lou, *Adv. Mater.*, 2017, **29**, 39.
7 X. B. Xu, Z. C. Zhang and X. Wang, *Adv. Mater.*, 2015, **27**, 5365–5371.
8 D. Luo, G. R. Li, Y.-P. Deng, Z. Zhang, J. D. Li, R. L. Liang, M. Li, Y. Jiang, W. W. Zhang, Y. S. Liu, W. Lei, A. P. Yu and Z. W. Chen, *Adv. Energy Mater.*, 2019, **9**, 1900228.
9 C. C. Nguyen, N. N. Vu and T. O. Do, *J. Mater. Chem. A*, 2015, **3**, 18345–18359.
10 Y. Zhao, L. N. Lin, Y. Lu, S. F. Chen, L. A. Dong and S. H. Yu, *Adv. Mater.*, 2010, **22**, 5255–5259.
11 B. Y. Guan, A. Kushima, L. Yu, S. Li, J. Li and X. W. Lou, *Adv. Mater.*, 2017, **29**, 1605902.
12 J. Zhang, J. W. Wan, J. Y. Wang, H. Ren, R. B. Yu, L. Gu, Y. L. Liu, S. H. Feng and D. Wang, *Angew. Chem., Int. Ed.*, 2019, **58**, 5266–5271.
13 S. M. Xu, C. M. Hessel, H. Ren, R. B. Yu, Q. Jin, M. Yang, H. J. Zhao and D. Wang, *Energy Environ. Sci.*, 2014, **7**, 632–637.
14 Y. Lu, L. Yu, M. H. Wu, Y. Wang and X. W. (David) Lou, *Adv. Mater.*, 2018, **30**, 1702875.
15 Y. W. Wang, L. Yu and X. W. (David) Lou, *Angew. Chem., Int. Ed.*, 2016, **55**, 14668–14672.
16 T. G. Mason, J. N. Wilking, K. Meleson, C. B. Chang and S. M. Graves, *J. Phys.: Condens. Matter*, 2006, **18**, R635–R666.
17 Z. H. Dong, X. Y. Lai, J. E. Halpert, N. L. Yang, L. X. Yi, J. Zhai, D. Wang, Z. Y. Tang and L. Jiang, *Adv. Mater.*, 2012, **24**, 1046–1049.
18 X. Y. Lai, J. Li, B. A. Korgel, Z. H. Dong, Z. M. Li, F. B. Su, J. A. Du and D. Wang, *Angew. Chem., Int. Ed.*, 2011, **50**, 2738–2741.
19 Z. H. Dong, H. Ren, C. M. Hessel, J. Y. Wang, R. B. Yu, Q. Jin, M. Yang, Z. D. Hu, Y. F. Chen, Z. Y. Tang, H. J. Zhao and D. Wang, *Adv. Mater.*, 2014, **26**, 905–909.
20 W. Li, P. Xu, H. C. Zhou, L. R. Yang and H. Z. Liu, *Sci. China: Technol. Sci.*, 2012, **55**, 387–416.
21 X. Fan, Z. Zhang, G. Li and N. A. Rowson, *Chem. Eng. Sci.*, 2004, **59**, 2639–2645.

22 H. L. Xu and W. Z. Wang, *Angew. Chem., Int. Ed.*, 2007, **46**, 1489–1492.
23 Q. Zhang, J. P. Ge, J. Goebl, Y. X. Hu, Z. D. Lu and Y. D. Yin, *Nano Res.*, 2009, **2**, 583–591.
24 Q. Zhang, W. S. Wang, J. Goebl and Y. D. Yin, *Nano Today*, 2009, **4**, 494–507.
25 Y. X. Hu, J. P. Ge, Y. G. Sun, T. R. Zhang and Y. D. Yin, *Nano Lett.*, 2007, **7**, 1832–1836.
26 Y. G. Sun, B. T. Mayers and Y. N. Xia, *Nano Lett.*, 2002, **2**, 481–485.
27 Y. N. Xia, Y. J. Xiong, B. Lim and S. E. Skrabalak, *Angew. Chem., Int. Ed.*, 2009, **48**, 60–103.
28 C. M. Cobley and Y. N. Xia, *Mater. Sci. Eng., R*, 2010, **70**, 44–62.
29 C. C. Yec and H. C. Zeng, *J. Mater. Chem. A*, 2014, **2**, 4843–4851.
30 H. C. Zeng, *Curr. Nanosci.*, 2007, **3**, 177–181.
31 L. P. Zhu, H. M. Xiao, W. D. Zhang, G. Yang and S. Y. Fu, *Cryst. Growth Des.*, 2008, **8**, 957–963.
32 Y. D. Yin, R. M. Rioux, C. K. Erdonmez, S. Hughes, G. A. Somorjai and A. P. Alivisatos, *Science*, 2004, **304**, 711–714.
33 W. S. Wang, M. Dahl and Y. D. Yin, *Chem. Mater.*, 2013, **25**, 1179–1189.
34 H. J. Fan, U. Gosele and M. Zacharias, *Small*, 2007, **3**, 1660–1671.
35 S. Kitagawa, R. Kitaura and S.-i. Noro, *Angew. Chem., Int. Ed.*, 2004, **43**, 2334–2375.
36 S. R. Batten, N. R. Champness, X. M. Chen, J. G. Martine, S. Kitagawa, L. Öhrström, M. O'Keeffe, M. P. Suh and J. Reedijk, *Pure Appl. Chem.*, 2013, **85**, 1715–1724.
37 C. Janiak, *J. Chem. Soc., Dalton Trans.*, 2003, 2781–2804.
38 B. Y. Guan, A. Kushima, L. Yu, S. Li, J. Li and X. W. Lou, *Adv. Mater.*, 2017, **29**, 1605902.
39 W. Cho, Y. H. Lee, H. J. Lee and M. Oh, *Adv. Mater.*, 2011, **23**, 1720–1723.
40 L. L. Hu, B. H. Qu, C. C. Li, Y. J. Chen, L. Mei, D. N. Lei, L. B. Chen, Q. H. Li and T. H. Wang, *J. Mater. Chem. A*, 2013, **1**, 5596–5602.
41 L. F. Shen, L. Yu, X. Y. Yu, X. G. Zhang and X. W. Lou, *Angew. Chem., Int. Ed.*, 2015, **54**, 1868–1872.
42 N. Joshi, L. F. da Silva, H. S. Jadhav, F. M. Shimizu, P. H. Suman, J.-C. M'Peko, M. O. Orlandi, J. G. Seo, V. R. Mastelaro and O. N. Oliveira Jr., *Sens. Actuators, B*, 2018, **257**, 906–915.
43 J. F. Marco, J. R. Gancedo, M. Gracia, J. L. Gautier, E. I. Rios and H. M. Palmer, *J. Mater. Chem.*, 2001, **11**, 3087–3093.
44 Y. Sharma, N. Sharma, G. V. S. Rao and B. V. R. Chowdari, *Adv. Funct. Mater.*, 2007, **17**, 2855–2861.
45 W. Luo, X. L. Hu, Y. M. Sun and Y. H. Huang, *J. Mater. Chem.*, 2012, **22**, 8916–8921.
46 J. Maier, *Nat. Mater.*, 2005, **4**, 805–815.
47 Y. F. Zhukovskii, P. Balaya, E. A. Kotomin and J. Maier, *Phys. Rev. Lett.*, 2006, **96**, 4.
48 P. Balaya, H. Li, L. Kienle and J. Maier, *Adv. Funct. Mater.*, 2003, **13**, 621–625.
49 X. Y. Lai, J. E. Halpert and D. Wang, *Energy Environ. Sci.*, 2012, **5**, 5604–5618.
50 J. Qi, X. Y. Lai, J. Y. Wang, H. J. Tang, H. Ren, Y. Yang, Q. Jin, L. J. Zhang, R. B. Yu, G. H. Ma, Z. G. Su, H. J. Zhao and D. Wang, *Chem. Soc. Rev.*, 2015, **44**, 6749–6773.